Structure and function of redox-sensitive superfolder green fluorescent protein variant

Kim C. Heimsch¹, Christoph G. W. Gertzen^{2,3}, Anna Katharina Schuh¹, Thomas Nietzel⁵, Stefan Rahlfs¹, Jude M. Przyborski¹, Holger Gohlke^{2,4}, Markus Schwarzländer⁵, Katja Becker¹, Karin Fritz-Wolf^{1,6*}

¹Biochemistry and Molecular Biology, Interdisciplinary Research Center, Justus Liebig University Giessen, 35392 Giessen, Germany

²Institute of Pharmaceutical and Medicinal Chemistry, Heinrich Heine University Düsseldorf, 40225 Düsseldorf, Germany

³Center for Structural Studies (CSS), Heinrich Heine University Düsseldorf, 40225 Düsseldorf, Germany

⁴John von Neumann Institute of Computing (NIC), Jülich Supercomputing Centre (JSC), Institute of Biological Information Processing (IBI-7: Structural Biochemistry), and Institute of Bio- and Geosciences (IBG-4: Bioinformatics), Forschungszentrum Jülich GmbH, 52428 Jülich

⁵Institute of Plan Biology and Biotechnology, University of Münster, 48143 Münster, Germany

⁶Max-Planck Institute of Medical Research, 69120 Heidelberg, Germany

Competing interests: the authors have declared that no competing interests exist.

*Corresponding author e-mail: karin.fritz@mr.mpg.de

Keywords: GFP, genetically encoded biosensors, X-ray crystal structure, molecular dynamics simulation, redox regulation, Plasmodium falciparum

Running title: Structure and function of redox-sensitive superfolder green fluorescent protein variant

Word count: 4,834

Reference numbers: 73

Number of greyscale illustrations: 6

Number of color illustrations: 9

Abstract

Aims: Genetically encoded GFP-based redox biosensors are widely used to monitor specific and dynamic redox processes in living cells. Over the last years, various biosensors for a variety of applications were engineered and enhanced to match the organism and cellular environments, which should be investigated. In this context, the unicellular intraerythrocytic parasite *Plasmodium*, the causative agent of malaria, represents a challenge, as the small size of the organism results in weak fluorescence signals that complicate precise measurements, especially for cell compartment-specific observations. To address this, we have functionally and structurally characterized an enhanced redox biosensor superfolder roGFP2 (sfroGFP2).

Results: SfroGFP2 retains roGFP2-like behavior, yet with improved fluorescence intensity in cellulo. SfroGFP2-based redox biosensors are pH-insensitive in a physiological pH range and show midpoint potentials comparable to roGFP2-based redox biosensors. Using crystallography and rigidity theory, we identified the superfolding mutations as being responsible for improved structural stability of the biosensor in a redox-sensitive environment, thus explaining the improved fluorescence intensity in cellulo.

Innovation: This work provides insight into the structure and function of GFP-based redox biosensors. It describes an improved redox biosensor (sfroGFP2) suitable for measuring oxidizing effects within small cells where applicability of other redox sensor variants is limited.

Conclusion: Improved structural stability of sfroGFP2 gives rise to increased fluorescence intensity *in cellulo*. Fusion to hGrx1 provides the hitherto most suitable biosensor for measuring oxidizing effects in *Plasmodium*. This sensor is of major interest for studying glutathione redox changes in small cells, as well as subcellular compartments in general.

4

The green fluorescent protein (GFP) isolated from the jellyfish $Aequorea\ victoria^{51,66}$, possesses a p-hydroxybenzylidene-imidazolidinone chromophore, which is formed upon internal cyclization and oxidation of the three amino acids (AA) Ser, Tyr, and Gly¹⁹. Dependent on the protonation/ionization state of the chromophore, GFP has two

excitation maxima, at 395 nm and 475 nm, both giving rise to emission with a maximum at

508 nm 3,66 . Due to the β -barrel structure of GFP, the chromophore is largely shielded from surrounding solvents 3 . Over the years, the spectral properties of the original wild type (WT) avGFP ($Aequorea\ victoria\ GFP$) have been optimized through protein engineering. In nature, WT avGFP associates aequorin, involving hydrophobic interaction of the protein surfaces; absence of aequorin can cause aggregation. The so-called cycle 3 mutations (F99S, M153T, V163A) result in more hydrophilic residues, reduce aggregation, and improve chromophore activation 8 . Including these resulted in a GFP version with a stronger fluorescence signal was generated; however, excitation maxima remained

unchanged⁸. Additional mutations (F64L, S65T) in combination lead to an increase in

fluorescence intensity (FI) compared to WT avGFP^{7,70}. Pédelacq et al. added further

mutations (S30R, Y39N, N105T, Y145F, I171V, and A206V) to generate superfolder GFP.

Those mutations lead to improved thermodynamic stability, faster folding, and decreased folding interference⁴⁵. Besides using GFP as a fluorescence reporter in a wide range of cell biological applications, it has also been utilized to generate a redox-sensitive biosensor that allows ratiometric, real-time measurements in living cells. By inserting cysteine pairs

into juxtaposed β -strands of the GFP barrel surface, spectral changes of the chromophore are dependent on alterations in redox potential of redox couples that are able to react and equilibrate with the thiol/disulfide redox switch¹⁸. The two excitation maxima of roGFP (reduction/oxidation-sensitive green fluorescent protein) are shifted to about 400 nm and 490 nm¹⁸.

We have previously used GFP-based redox biosensors to study oxidizing effects within *Plasmodium falciparum* parasites^{32,64}, which replicate within mature human red blood cells. Malaria parasites encounter oxidative challenge, e.g. due to the parasite's high metabolic rate, from products of red blood cell hemoglobin digestion during the

intraerythrocytic life cycle and the immune responses of the host²⁸. Furthermore, it is known that some antimalarials mediate their effect at least partially by increasing the production rates of reactive oxygen species (ROS) and of other free radicals³³. Therefore, studying changes in the redox metabolism of *Plasmodium* parasites is of considerable interest to understand the mode of action of new antimalarials, as well as resistance mechanisms. The small size of *Plasmodium* parasites (2-5 µm in the asexual erythrocytic stages usually studied) has been technically challenging for fluorimetry and imaging approaches, as well as the high background pigmentation of the host cell. Membrane-bound sub-compartments of the parasites (apicoplast, mitochondrion, parasitophorous vacuole) are even smaller, further complicating precise measurement of cellular parameters. Fluorescence signals of commonly used redox biosensors regularly result in comparatively worse signal-to-noise ratios, further complicating the situation. This is even more the case for measurements in subcellular compartments with small volume such as the mitochondrial matrix.

In previous work, the two cysteines S147C and Q204C, as well as the F223R mutation from roTurbo¹³, were included in sfGFP, resulting in sfroGFP2 (superfolder reduction/oxidation-sensitive GFP 2, sfroGFP2^{WT}), which showed strongly increased FI *in cellulo*⁶⁴ (Figure 1).

In this study, we characterized sfroGFP2 to assess its functionality in *Plasmodium* parasites. We presented a X-ray crystal structure resolved to 1.1 Å and used this as a basis to examine the structural stability of the protein further. Structural stability can be probed by modeling the structures as constraint networks, where atoms as nodes are connected by constraints due to covalent and non-covalent bonds, and via subsequent analysis based on a rigidity theory^{24,49,50,55}. We tested the hypothesis that the improved fluorescence and robustness of sfroGFP2^{WT} may be related to a higher structural stability of this variant⁴⁶.

To gain empirical insights into the relative contribution of specific residues to the modified structural and functional properties of sfroGFP2^{WT}, we removed specific superfolding mutations, namely S30R, Y39N, and F223R. Based on the crystal structure of sfroGFP2^{WT} it is very unlikely that the both sf mutations Y147F and I171V influences the structure to any major extend. Furthermore, as already stated by Pédelacq and colleagues, the N105T side chain does not affect the orientation of the adjacent residue side chains. In sfGFP the

mutation A206V comes into close contact with the phenyl group of F223⁴⁵. However, since the AA at position 223 points towards the solvent phase, we did not assume an impact to the structural stability. We have therefore focused our examinations on the both sf mutations S30R and Y39N and did not focus on any of the other sf mutations, since we did not assume major effects to the structure of the sensor.

Gutscher and colleagues fused roGFP to human glutaredoxin-1 (hGrx1), thereby generating a proximity-based biosensor that specifically equilibrates with the glutathione couple, thus overcoming uncertainties about the *in vivo* specificity of the free roGFP biosensor, as well as slow responsiveness^{17,18}. Taking our lead from this, we have here fused sfroGFP2^{WT} to hGrx1, combining the advantages of a specific and fast responding biosensor resulting from hGrx1-fusion with the increased FI of sfroGFP2^{WT}.

Results

The improved redox biosensor sfroGFP2^{WT} shares 94% sequence identity with *av*GFP. It contains all roGFP2 substitutions plus the sf (superfolding) mutations⁴⁵ (Figure 2A), as well as F223R¹³. This sensor was recently published by our research group and showed favorable properties as compared to the commonly used roGFP2 variant when used *in cellulo*⁶⁴.

To determine whether the two specific sf mutations S30R and Y39N are involved in increasing the stability of sfroGFP2^{WT} compared to roGFP2, we reversed these two mutations, as well as F223R, one at a time. We investigated the three reversion mutants (mutants are called throughout the manuscript as follows: sfroGFP2^{R30S}, sfroGFP2^{N39Y}, and sfroGFP2^{R223F}), as well as sfroGFP2^{WT} and the fusion sensor hGrx1-sfroGFP2, in comparison to roGFP2 and hGrx1-roGFP2, by using a set of complementary methods we: (i) determined and analyzed the crystal structures of sfroGFP2^{WT}, sfroGFP2^{R30S}, and sfroGFP2^{N39Y}; (ii) performed rigidity analysis for sfroGFP2^{WT} and a set of different models based on it; and (iii) assessed the spectral and functional properties of all roGFP2 and sfroGFP2^{WT}-based biosensors.

Crystal structure analysis

We obtained orthorhombic and monoclinic crystals of sfroGFP2 WT . The sfroGFP2 WT protein crystallizes in space group P2₁2₁2₁ and contains one monomer in the asymmetric unit. SfroGFP2 R30S and sfroGFP2 N39Y obey P2₁ symmetry, with two or four monomers in the asymmetric unit, respectively. The sfroGFP2 WT crystal diffracted to a resolution of 1.1 Å and the mutants sfroGFP2 R30S and sfroGFP2 N39Y to 1.4 Å and 2.0 Å, respectively. All structures were solved via molecular replacement. Data collection and refinement statistics of all datasets are summarized in Table 1.

The sfroGFP2 $^{\text{WT}}$ monomer (238 AA) adopts the canonical GFP fold, which comprises an eleven-stranded β -barrel with an inner α -helix, containing the covalently bound chromophore 4-(p-hydroxybenzylidene)imidazolidine-5-one (Figure 2A). In our structures the two cysteines C147 and C204, which are able to respond to the ambient redox environments and fundamental for the use of roGFP variants as redox sensors, form a disulfide bridge.

All sf mutations are located on the surface of the barrel. Two of the sf mutations (S30R, Y39N) are of particular interest because they give rise to novel interactions between neighboring β -strands. In sfroGFP2^{WT}, residues R30 and N39 form hydrogen bonds to D19 and D36, respectively (Figure 2A); these interactions do not occur in roGFP2. For the F223R mutation, we did not expect any effect on the X-ray structure because R223 points towards the solvent phase (Figure 2A) and is unlikely to interact with other amino acids. For this reason, we focused our efforts on the sfroGFP2^{R30S} and sfroGFP2^{N39Y} variants.

As mentioned above, the sfroGFP2^{WT}, sfroGFP2^{R30S}, and sfroGFP2^{N39Y} structures contain one, two, and four monomers of sfroGFP2 in the asymmetric unit, respectively. The seven monomers are similar, with rmsd (root-mean-square deviation) values of 0.3 to 0.8 Å with 228 C α atoms. Differences occur at the N-terminus and in the location of a surface loop (8-11) (Figure 2B). However, this region is involved in monomer–monomer interactions of the mutants and seem unlikely to be relevant for the stability properties of sfroGFP2^{WT}.

In the sfroGFP2^{WT} structure, there is an ion pair network in the vicinity of R30 that involves four neighboring strands of the β -barrel. R30, located centrally on a β -strand (β 2, figure 3),

interacts with D19 from the adjacent strand ($\beta1$). The next strand ($\beta6$) is connected to $\beta1$ by a bond between E17 ($\beta1$) and R122 ($\beta6$). Moreover, R122 forms a salt bridge to E115 ($\beta5$) . Furthermore, E111 ($\beta5$) and K113 ($\beta5$) are connected by a bond. Therefore, the strands $\beta1$, $\beta2$, $\beta5$ and $\beta6$ are connected via a network of ionic interactions.

Superimposition of the four monomers from the sfroGFP2^{N39Y} structure reveals that the side chain of R30 (β 2) adopts different conformations in the subunits, thereby interacting with E32 (β 2) or E17 (β 1). The interaction between R122 (β 6) and E115 (β 5) is present in all four subunits, but only in two sfroGFP2^{N39Y} monomers (A, B) does R122 (β 6) also interact with E17 (β 1). K113 also adopts several conformations, but only in one subunit (D) does it interact with another residue (E115, β 5) (Figure 3).

Due to the reversed R30S ($\beta2$) mutation in sfroGFP2^{R30S}, the much smaller sidechain of S30 is not able to interact with residues D19 ($\beta1$) or E32 ($\beta2$); instead, S30 interacts with E17 ($\beta1$) through a hydrogen bond. Due to the high strength of this interaction, the E17 side chain adopts a completely different conformation from that seen in the sfroGFP2^{WT}—or the four sfroGFP2^{N39Y}—structures. Consequently, R122 ($\beta6$) is no longer able to connect strands $\beta1$ and $\beta6$ (Figure 3).

In the sfroGFP2^{WT} structure, N39 interacts with D36 through a hydrogen bond (Figure 2A); in the sfroGFP2^{N39Y} structure, Y39 points into the solvent (Figure 2B). Of interest is the small apparent shift of the chromophore within the barrel by about 0.2 Å in the sfroGFP2^{R30S} and 0.3 Å in the sfroGFP2^{N39Y} structures. However, since the coordinate errors are almost as large, the shift cannot be resolved with any certainty.

Larger differences are seen in the network of ionic interactions within the three variants. The most complex ion network is formed in the sfroGFP2^{WT}, which therefore presumably contributes to a higher structural stability of the protein.

Rigidity analysis

To obtain dynamic structural information as a direct link to the functional properties of the protein, we next used the X-ray crystal structure of sfroGFP2^{WT} as a template to perform rigidity analysis. We inserted the relevant substitutions to create structural models of GFP

(GFP $_{sfroGFP2}$) and roGFP2 (roGFP2 $_{sfroGFP2}$) to explore differences in stability between these variants. Furthermore, the structural models R30S $_{sfroGFP2}$, N39Y $_{sfroGFP2}$, and R223F $_{sfroGFP2}$ were generated based on the sfroGFP2 WT template to investigate residue-specific effects.

We hypothesized that the higher FI of sfroGFP2^{WT} in an *in cellulo* environment is associated with the higher structural stability of sfroGPF2^{WT} compared to GFP. To test this hypothesis we analyzed the different structures with respect to their mechanical stability. We applied principles from rigidity theory. Details about these computations are provided in the Methods section.

The computations predict that the major phase transition of sfroGFP2^{WT} (E_{cut} = -4.01 kcal mol⁻¹) occurs at an energy E_{cut} 0.13 kcal mol⁻¹ lower than that of GFP_{sfroGFP2} (E_{cut} = -3.88 kcal mol⁻¹) (Figure S1; Table 2; p = 0.13; two-sided t-test, n = 5), with both variants showing one major phase transition (Figure S2A, C). The result clearly indicates a higher structural stability of sfroGFP2^{WT} than GFP.

To obtain insights at the local, residue-wise level, the averaged constraint dilution trajectory of GFP_{sfroGFP2} (Figure 4A) was visually inspected, revealing that—except for residue 30—all residues that are exchanged via sf mutations in sfroGFP2^{WT} segregate from the giant rigid cluster right before the major phase transition (Figure 5A). Hence, these residues are structural weak spots that, when appropriately substituted, should increase the structural stability by shifting the phase transition to lower E_{cut} values. Indeed, in sfroGFP2^{WT}, the substituted residues segregate at a later point in the constraint dilution trajectory (Figure 4B).

The sf mutation S30R in sfroGFP2^{WT}, which forms a hydrogen bond with D19 in the neighboring β -strand, segregates from the largest rigid cluster during the major phase transition (Figure 5B). Hence, this interaction is particularly important for the structural integrity of sfroGFP2^{WT}. The importance of R30 in sfroGFP2^{WT} is corroborated in that the phase transition of R30S_{sfroGFP2} is at an E_{cut} value 0.11 kcal mol⁻¹ higher than that of sfroGFP2^{WT} (Figure S1, Table 2, p = 0.10) and on a par with that of GFP (Figure S1, Table 2). Accordingly, reversing this substitution abolishes most of the gain in the structural stability of sfroGFP2^{WT} over GFP. The particular effect of residue 30 is dependent on the residue

composition of sfroGFP2^{WT}, however (Figure 5B). In roGFP2_{sfroGFP2}, which contains S30 from GFP and none of the other sf mutations, yet is similarly resistant to oxidation like sfroGFP2^{WT}, the major phase transition occurs at almost the same E_{cut} as in sfroGFP2^{WT} (Figure S1, Table 2). Apparently, the roGFP2 mutations have a different long-range effect based on the changing interactions of the residues in the presence or absence of the sf mutations. In turn, the interactions formed by the sf mutations in sfroGFP2^{WT} alter the constraint network due to interaction partners changing conformation to accommodate the mutations (Figure 5B). By contrast, N39Y_{sfroGFP2} and R223F_{sfroGFP2} behave similarly to sfroGFP2^{WT} (Figure S1, Table 2).

The rigidity percolation behavior of protein networks is usually complex, and multiple phase transitions can be observed 44,57 . In line with this, besides a shift of the major phase transition point, substitutions in sfroGFP2 also impact later transitions in the constraint dilution trajectory. In GFP_{sfroGFP2}, the last rigid part of the protein is part of the β -barrel and comprises residues T95-F97, F163, K164, and D178-Y180 (Figure 4A); by contrast, in sfroGFP2 the last rigid part of the protein is the fluorophore (Figure 5C).

These analyses of structural stability reveal a later rigid-to-flexible phase transition during constraint dilution simulations in sfroGFP2 WT than in GFP, pinpoint the particular role of the S30R substitution, and suggest that sf mutations increase not only the structural stability of the β -barrel but also of the fluorophore region. To examine the effects of the sf mutations on the biosensors' properties, we performed functional characterization.

Functional properties

Spectral excitation scans were recorded using recombinant sfroGFP2^{WT}, the three reverse mutants sfroGFP2^{R30S}, sfroGFP2^{N39Y}, and sfroGFP2^{R223F}, as well as roGFP2, which served as a reference (Figure 6A). Fluorescence spectra of roGFP2 (Figure 6A) were consistent with previously published spectral scans^{18,65}. As shown in Figure 6A, the different sf mutations did not affect the dual excitation behavior. For oxidized protein, excitation peaks at 405 nm and 485 nm are seen. However, the excitation peak at 485 nm is stronger for reduced protein. Therefore, the commonly used excitation maxima for roGFP-based redox measurements can be used identically for sfroGFP2^{WT} and sfroGFP2-based redox

biosensors. Furthermore, the emission scans (Figures S3 and S4) for all investigated biosensors showed the same emission pattern with maxima at 510 nm (data not shown). These results confirm that the sf mutations do not affect the excitation and emission pattern of the sensors. The isosbestic point (λ_{iso}) , which represents the excitation wavelength at which the sensor fluorescence is unresponsive to redox changes, was identified at λ_{iso} = 422 nm for roGFP2, consistent with previous reports^{2,66}. The isosbestic points of sfroGFP2 WT and sfroGFP2 variants were slightly shifted toward lower wavelengths to about λ_{iso} = 415 nm (Figure 7A). Although the isosbestic point of sfroGFP^{WT} is closer to the lower wavelength excitation (typically 405 nm used for confocal microscopy) than the isosbestic point of roGFP2, a negative impact on the usability of the biosensor was not observed. In vitro spectral excitation scans using standard potassium phosphate buffer show slightly more intense fluorescence intensities (FI) for roGFP2 (FI_{ox405} = 25,000 RFU; $FI_{red485} = 100,000 \text{ RFU}$) than for sfroGFP2^{WT} ($FI_{ox405} = 16,000 \text{ RFU}$; $FI_{red485} = 87,000 \text{ RFU}$) (Figure 5A, light red and light blue spectra). Moreover, the FI of emission at 510 nm after excitation at 405 and 485 nm was slightly stronger for roGFP2 than for sfroGFP2 wt (roGFP2: $FI_{510ox} = 17,000 \text{ RFU}$, $FI_{510red} = 22,000 \text{ RFU}$; $sfroGFP2^{WT} FI_{510ox} = 11,000 \text{ RFU}$, $FI_{510red} = 11,000 \text{ RFU}$ = 19,000 RFU) (Figures S3 and S4).

Spectral excitation and emission scans of the reverse mutants sfroGFP2^{R30S}, sfroGFP2^{N39Y}, and sfroGFP2^{R223F} showed the same overall pattern as sfroGFP2^{WT}. All sfroGFP2 variants showed higher FI than sfroGFP2^{WT} in vitro for both excitation wavelengths as well as for emission at 510 nm after excitation at 405 nm and 485 nm. Additionally, sfroGFP2^{R30S} and sfroGFP2^{R223F} showed higher FI than roGFP2 (Figures 6A, S3, and S4).

Furthermore, spectral scans were recorded at physiological temperature (37 °C) to mimic the conditions for *in cellulo* measurements in *P. falciparum*, where structural stability may be particularly relevant to withstand increased thermal challenge (Figure 6A, dark red and dark blue spectra). With higher temperatures, the FI of roGFP2 and sfroGFP2^{WT} decreased. However, the reduction in FI was not as pronounced for sfroGFP2^{WT} as for roGFP2. The decrease in FI of emission at 510 nm with a higher temperature was more pronounced for roGFP2 than sfroGFP2^{WT} (Figures S3 and S4). Changes in FI of sfroGFP2^{R30S}, sfroGFP2^{N39Y},

and sfroGFP2^{R223F} were in a comparable range. The sharpest decline in FI_{405ox} was seen for sfroGFP2^{R223F}. The strongest decrease in FI_{485red} , was seen for sfroGFP2^{R30S}.

Following the rationale of proximity-based redox sensor specificity introduced by Gutscher *et al.*, sfroGFP2^{WT} was fused to hGrx1 to generate a proximity-based sensor that allows specific and fast equilibration between sfroGFP2^{WT} and the glutathione redox couple¹⁷. The fusion sensor hGrx1-sfroGFP2 was characterized in comparison to hGrx1-roGFP2. Spectral excitation and emission scans with recombinant biosensors were recorded at 10 °C (Figures 6B, S3, and S4, light red and light blue spectra). Here, hGrx1-roGFP2 showed higher FI than hGrx1-sfroGFP2. Additionally, spectral scans were performed at physiological temperature (37 °C) (Figure 6B, dark red and dark blue spectra). Here, the FI of hGrx1-roGFP2 decreased, whereas it increased for hGrx1-sfroGFP2. In general, FI were higher for both hGrx1-fusion sensors, i.e. roGFP2 and sfroGFP2^{WT}.

In order to study the spectral response of the sensor variants to oxidation and reduction, as well as the reversibility of the reaction, ratio changes with recombinant roGFP2, hGrx1-roGFP2, sfroGFP2^{WT}, and hGrx1-sfroGFP2 were measured. As shown in Figure S3, all biosensors responded rapidly to oxidation with diamide. The ratio of the fully oxidized biosensors was stable but could be fully reversed via reduction with dithiothreitol. No difference in the responsiveness to oxidizing and reducing agents was identified between the individual biosensor variants tested.

We examined the pH responsiveness for all redox biosensors. These responses were monitored over a pH range from 5.0 to 9.0 to cover physiologically meaningful conditions. The ratios of all biosensors were unaffected by pH across the range from 6.0 to 8.0; only a minor impact started to become apparent at acidic pH values below 6.0 (Figure 7). That data confirm that pH insensitivity, as a major advantage of roGFP-based redox sensors is retained in the sensor variants.

Redox titrations were performed for all redox biosensors, using the DTT/dithian system, to determine the midpoint potentials (Figure 8). Midpoint potentials for roGFP2 have been empirically determined and vary somewhat depending on the specific protocol used (-272 mV vs. -284 mV). Therefore, a consensus midpoint potential of roGFP2 was defined at -280 mV^{12,18,39}. Our results are in accordance with this as the midpoint potential of roGFP2

within our measurements was -280.3 \pm 0.4 mV. Moreover, we found that the different sf mutations did not change the midpoint potential of the sensor to any major extent as the midpoint potential of sfroGFP2^{WT} is -283.6 \pm 0.5 mV. The midpoint potentials of hGrx1 fusion and the other sensor variants are also largely retained and are only slightly more negative; with -287.1 \pm 0.4 mV for hGrx1-roGFP2, -285.8 \pm 0.4 mV for hGrx1-sfroGFP2, -283.9 \pm 0.2 mV for sfroGFP2^{R30S}, -286.8 \pm 0.7 mV for sfroGFP2^{N39Y}, and -284.8 \pm 0.4 mV for sfroGFP2^{R223F}.

In cellulo use of redox biosensors

SfroGFP2^{WT} was stably integrated into the genome of NF54*attB Plasmodium falciparum* clone (P. falciparum) through integrase-mediated homologous recombination between the parasite's attB site and the plasmid's attP site 43 as already described by Schuh et al. 64 . Spectral excitation scans of NF54attB^{sfroGFP2} showed normal roGFP behavior with strong FI and an improved signal-to-noise ratio (Supplementary Figure S4). These results are in agreement with earlier published data⁶⁴. Furthermore, we stably integrated the fusion sensor hGrx1-sfroGFP2 into the genome of NF54attB P. falciparum parasites because it was shown that the equilibration between sfroGFP2 with the glutathione couple is faster in different cellular contexts and the kinetics is standardized when the sensor is fused to glutaredoxin^{17,64}. For comparison, we used an NF54*attB* parasite line stably expressing hGrx1-roGFP2⁶⁴. Lines are referred to as NF54*attB*^{hGrx1-sfroGFP2} and NF54*attB*^{hGrx1-roGFP2} throughout the manuscript. All parasite lines used in this study expressed the sensors cytosolic. As shown in Figure 8, FI for NF54attB^{hGrx1-sfroGFP2} was strongly increased when compared to NF54attB^{hGrx1-roGFP2}. Wild type NF54attB parasites were used to adjust the FI by subtracting the background fluorescence of the parasites and the surrounding red blood cell. A difference in FI between in vitro and in cellulo measurements is clearly visible here. While the spectral properties of the recombinant sfroGFP2^{WT} do not seem to be better, the measurements with parasites show a clearly improved FI. This data shows an improved signal-to-noise ratio and an enhanced FI of sfroGFP2-based biosensors over roGFP2-based biosensors in cellulo.

Since the FI of both hGrx1-sfroGFP2 and sfroGFP2^{WT} was about 3x higher than that of hGrx1-roGFP2 *in cellulo*, (Figure 8; Supplementary Figure S4) while both sensor proteins

showed similar FI *in vitro* (Figure 6), we hypothesized that more mature and functional sf sensor protein was present due to enhanced expression, proportion of maturation, or stability. To test this hypothesis, Western blot (WB) analysis was performed to examine the expression levels of the different sensors. NF54 $attB^{hGrx1-roGFP2}$, NF54 $attB^{sfroGFP2}$, and NF54 $attB^{hGrx1-sfroGFP2}$ parasites were examined. All investigated proteins of interest were detected in full length. All samples showed a GFP signal with the expected size (Supplementary Figure S5). Band intensity between the samples NF54 $attB^{hGrx1-roGFP2}$ and NF54 $attB^{hGrx1-roGFP2}$ differed by -2.3% \pm 11.2%. The difference in band intensity between the samples NF54 $attB^{hGrx1-roGFP2}$ and NF54 $attB^{hGrx1-roGFP2}$ was -28.7% \pm 20.8%. Anti-PfHSP70 antibody was used as a loading control (Supplementary Figure S5). This analysis showed that expression levels between the sensors only differed slightly, with NF54 $attB^{hGrx1-roGFP2}$ showing the highest expression level. Thus, degree of maturation and/or stability of folding, as indicated by the rigidity analysis of sensor structure, appears to be responsible for the improved *in cellulo* performance rather than protein abundance.

Discussion

In this work, we aimed to identify the molecular basis for the improved fluorescence properties of sfroGFP2^{WT} as this knowledge provides important insights for future sensor developments. To achieve this goal, we characterized different redox biosensor variants *in vitro* and *in cellulo*.

In previous studies in which we described the redox biosensor sfroGFP2^{WT}, we demonstrated an improved FI *in cellulo*⁶⁴, which could be confirmed in this study. *Plasmodium falciparum* parasites stably expressing sfroGFP2^{WT} or hGrx1-sfroGFP2 showed improved FI compared to parasites expressing hGrx1-roGFP2. Enhanced expression levels of (hGrx1)-sfroGFP2 could be excluded as a cause of the improved FI via Western blot analysis as the expression levels of all sensor proteins investigated here were comparable. Subsequently, further *in vitro* investigations were carried out.

During the development of sfroGFP2^{WT}, we aimed to improve the FI of the redox biosensor, but without affecting other sensor properties. We therefore investigated the pH responsiveness of the different sensor variants and determined their midpoint potential.

All redox biosensor variants are pH insensitive at physiologically meaningful pH values

between pH 6.0 and 8.0 and show midpoint potentials similar to roGFP2-based biosensors, making them suitable sensors for measuring oxidizing effects within the cytosol and most of the subcellular compartments of *Plasmodium* parasites. *In cellulo*, the use of sfroGFP2^{WT} fused to hGrx1 seems to be wiser, since it allows reactions with GSH and GSSG to proceed much more effectively⁶⁴.

Unexpectedly, *in vitro* spectral scans showed a diminished FI for recombinant (hGrx1)-sfroGFP2^{WT} compared to recombinant (hGrx1)-roGFP2 using standard conditions. We investigated this effect in more detail and performed spectral scans at different temperatures. We observed a more stable FI for sfroGFP2-based biosensors at higher temperatures (37°C), which are required for *in cellulo* measurements with *Plasmodium* parasites. In general, the FI of both hGrx1-fusion sensors were higher. We therefore hypothesize a potentially stabilizing effect of hGrx1, improving the FI of the actual sensor. Stabilizing effects of Trx—which features Grx fold—have already been described³⁶. These advantageous properties are used for protein expression and purification. Here, Trx is used as a fusion protein to prevent protein aggregation and to increase the folding behavior of the protein of interest³⁶.

Protein–protein interactions occurring within the parasites could be excluded to be the only responsible factor for the differences in *in vitro* and *in cellulo* experiments. This was studied on the basis of spectral scans using recombinant protein equilibrated in buffer or parasite cell extract (data not shown). Nevertheless, the environment within an intact parasite differs strongly from standard buffer or lysed parasites. The concentration of different molecules as well as their interaction with each other or with membranes cannot be fully remodeled *in vitro*. As discussed by Minton and colleagues, molecular crowding can lead to large differences between *in vitro* and *in vivo* measurements^{40,59}. However, not only the surrounding cellular milieu can differ; furthermore, different host cells used for expression can also influence protein stability and their properties¹¹. Therefore, findings from *in vivo* or *in cellulo* measurements cannot always be explained with *in vitro* examinations.

For fluorescent proteins, the structural stability of the fluorophore is especially important to maintain the conjugated π -electron system and the dipole moment, which are

important for fluorescence³⁵. Therefore, we examined differences in structural stability between roGFP2 and sfroGFP2^{WT} using X-ray crystal structure analysis and rigidity analysis.

Our results, based on rigidity analysis, demonstrate that both roGFP2 and $sfroGFP2^{WT}$ show an improved structural stability over GFP. However, the sf mutations in sfroGFP2 WT lead to a different conformation of residues than in roGFP2, resulting in disparate interaction networks between the two variants. Pédelacq et al. have already suggested that among all sf mutations, S30R and Y39N have the greatest impact on folding stability 45. We have studied the effects of these specific sf mutations on protein stability in more detail by reversing them in the crystal structures of sfroGFP2^{R3OS} and sfroGFP2^{N39Y}, as well as their models R30S_{sfroGFP2} and N39Y_{sfroGFP2}, for rigidity analysis. We focused our efforts on these specific mutations and their impact on the protein stability. However, one has to mention that for roGFP-biosensors the H-bond involving E222 has also a major impact on the chromophore. Due to the S65T mutation, which is present in all redox biosensors derived from enhanced GFP, the H-bond network that stabilizes the neutral chromophore is disrupted, leading to a shift in equilibrium towards the anionic from. In roClover, a redox biosensor variant that includes the sf mutations as well, the conformation of E222 differs slightly. However this is not because of the sf mutations. Moreover the both mutations T65G and T203H present in roClover – but not roGFP2 nor sfroGFP2^{WT} – are rather responsible therefore. However, these specific mutations have the same effect than S65T that is present in both roGFP2 and sfroGFP2^{WT 4}. We therefore focused on the sf mutations S30R and Y39N. Our crystal structures of sfroGFP2^{WT} show that the barrel and the chromophore are at most marginally shifted in their position but an ion network between the strands is formed by inclusion of the sf mutation S30R, which probably increases the stability of sfroGFP2^{WT}. Even though both sf mutations cause an interaction between amino acids of adjacent strands, probably improving the stability of the barrel, we assume that the influence of the substitution at position 30 is much more critical than that at position 39 due to the more complex network in the surrounding of residue 30. Our sfroGFP2^{R3OS} and sfroGFP2^{N39Y} structures confirm these findings; in particular, reversing the sf mutation S30R in the crystal structure of sfroGFP2^{R30S} disrupts the ion pair network between adjacent strands. Even though we only saw slight structural differences between

our crystal structures of sfroGFP2^{WT} and sfroGFP2^{R3OS}, by using rigidity analysis, we were able to confirm that the sf mutation S30R is important for the stability of sfroGFP2^{WT}.

Reversing the sf mutation S30R in the structural model R30S_{sfroGFP2} has a major impact on the overall stability of the protein, reducing the stability close to the level of GFP.

Besides stabilizing the β -barrel structure, the sf mutations in sfroGFP2^{WT} also exert a long-range effect on the barrel center such that the fluorophore remains structurally stable until the end of the constraint dilution simulations, whereas in GFP, the fluorophore becomes unstable.

Taken together, our data confirms the hypothesis that variants with a higher resilience against oxidative alterations have a more stable structure under the experimental conditions chosen. The constraint dilution simulations explain this higher structural stability of roGFP2 and sfroGFP2^{WT} over GFP on a per residue level, including the fluorophore in sfroGFP2^{WT}, and thus can rationalize the higher stability and FI of these variants in changing redox conditions. These findings were in line with other studies showing a higher resilience of more structurally stable proteins^{16,23,38,44,46}, although this relation is not undebated³¹.

The knowledge generated in this study about the molecular basis underlying the improved FI of sfroGFP2^{WT}-based redox biosensors *in cellulo* compared to roGFP2-based biosensors can be applied to other sensors and thus enrich the field of sensor development.

Innovation

The small size of *Plasmodium* parasites and their lifestyle, including their presence in highly pigmented erythrocytes make fluorescence-based measurement difficult. This is further complicated when measurements in subcellular compartments are to be performed. Generating a redox biosensor that shows improved FI *in cellulo* considerably enhances the quality of the measurement method (Figure 1). The deep structural and functional insight into the sensor properties gained by this study suggests that specific mutations can significantly improve the stability of a biosensor and thereby its *in cellulo* performance. This study provides a blueprint for rational optimization of biosensors to match specific biological requirements.

Materials and Methods

Drugs and chemicals

All chemicals used were of the highest available purity and were obtained from Thermo Fisher Scientific (Dreieich, Germany), Roth (Karlsruhe, Germany), Sigma-Aldrich (Steinheim, Germany), or Merck (Darmstadt, Germany). RPMI 1640 medium was purchased from Gibco (Paisley, United Kingdom) and SYBR Green I from Thermo Fisher Scientific (Dreieich, Germany).

Engineering sfroGFP2 mutants

To generate sfroGFP2^{R30S}, sfroGFP2^{N39Y}, and sfroGFP2^{R223F}, site-directed mutagenesis PCR was performed using pQE30-[sfroGFP2^{WT}] as a template, AccuPrimeTM Pfx DNA polymerase (ThermoFisher Scientific, Waltham, MA, USA), and specific primer pairs (Table S1). Template plasmids were digested using DpnI (ThermoFisher Scientific, Waltham, MA, USA). Correctness of mutants was verified by sequencing (LGC genomics).

Expression and purification of recombinant redox biosensors

The different redox biosensors were heterologously overexpressed using *E. coli* cells. RoGFP2 was expressed in lysogeny broth (LB) medium using *E. coli* M15 [pREP4] cells (kanamycin resistance, Kan^R), which were transformed with roGFP2 in pQE30 (carbenicillin resistance, Cn^R), at 37 °C for 4 h. HGrx1-roGFP2 was produced as described by Kasozi *et al.*³². SfroGFP2^{WT} and hGrx1-sfroGFP2 were produced according to Schuh *et al.*⁶⁴. For heterologous overexpression of the sfroGFP2 mutants, *E. coli* M15 [pREP4] cells (Kan^R) were transformed with either pQE30-[sfroGFP2^{R305}], pQE30-[sfroGFP2^{R223F}], or pQE30-[sfroGFP2^{N39Y}] (Cn^R, respectively). SfroGFP2^{R305} and sfroGFP2^{R223F} were expressed in LB medium at 37 °C or room temperature (RT) for 4 h. SfroGFP2^{N39Y} was expressed in terrific broth (TB) medium at 37 °C for 2 h. Pellets were harvested via centrifugation and stored at -20 °C. Frozen pellets were thawed, resuspended in HEPES buffer (50 mM Hepes, 300 mM NaCl, pH7.5), and mixed with protease inhibitors (150 nM pepstatin, 40 nM cystatin, 100 μM phenylmethylsulfonyl fluoride, PMSF). After lysis using lysozyme, DNase, and sonication, supernatants were obtained via centrifugation (18,000 rpm, 30 min, 4 °C). After purification of all proteins via hexahistidyl affinity chromatography on Ni-NTA and fast

protein liquid chromatography (FPLC), they were concentrated using 10 kDa or 30 kDa Vivaspin columns (Sarotius, Göttingen, Germany) and stored at 4 °C.

Crystallization, data collection, and processing of recombinant redox biosensors SfroGFP2^{WT}, sfroGFP2^{R30S}, and sfroGFP2^{N39Y} crystals were grown in white light at 22 °C in sitting drops with the vapor diffusion technique, using a Honeybee 961 crystallization robot. For crystallization of sfroGFP2^{WT}, the protein was concentrated in 300 mM NaCl and 0.05 M Hepes (pH 7.5) to 30 mg/ml. In the drop, 0.2 µl of protein solution was mixed with 0.2 μl reservoir solution (46% v/v EtOH, 0.25% v/v dichloromethane). Crystals appeared after one day at RT. Before data collection, crystal were soaked in mother liquor with a final concentration of 15% glycerol. Diffraction data for all crystals was collected at X10SA (detector: Pilatus) from the Swiss Light Source in Villigen, Switzerland. Diffraction data was collected at 100 K and processed with XDS³⁰. The orthorhombic crystals diffracted up to 1.1 Å resolution and obeyed P2₁2₁2₁ space group symmetry with one monomer in the asymmetric unit. SfroGFP2^{R30S} was crystalized using 0.2 µl of 30 mg/ml protein and 0.2 µl of 10% polyethylene glycol (PEG) 6000, 30% ethanol and 100 mM sodium acetate. After one day, crystals appeared at RT. The X-ray structure was solved with a resolution of 1.35 Å. For sfroGFP2 N39Y , 0.2 μ l of 30 mg/ml protein was mixed with 0.2 μ l 30% PEG 4000. Crystals appeared after five days. The structure was solved with a resolution of 2.0 Å.

Structure determination

The structure was solved via molecular replacement. The search model was generated via homology modeling with SWISS-MODEL⁷². As a template for modelling, we used the structure of *Aequorea victoria* GFP (Protein Data Bank (PDB) code 1qyo), which shares a sequence identity of 94% with sfroGFP2^{WT}. The first refinement of the molecular replacement solution revealed an Rfree of 25%. During refinement, 6% of all reflections were omitted and used for calculating an Rfree value. We improved the models in cycles of manual building and refinement, with a final Rfree of 16.2%. Data collection and refinement statistics are shown in Table 1. The PHENIX program suite¹ was used for reflection phasing and structure refinement. The interactive graphics program Coot¹⁴ was

used for model building. Molecular graphics images were produced using the UCSF Chimera package⁴⁷.

Rigidity analysis

Generation of structural models

The X-ray crystal structure of sfroGFP2^{WT} was used to generate structural models of R30S_{sfroGFP2}, N39Y_{sfroGFP2}, R223F_{sfroGFP2}, roGFP2_{sfroGFP2}, and GFP_{sfroGFP2}. The respective structural models were generated based on one template structure and with the same structural modeling technique to minimize these influences on the outcome of subsequent computations^{49,58}. This modeling was performed with Maestro as described below.

Molecular dynamics simulations

In all cases, Maestro (*Schrödinger, LLC, New York, USA,* 2017) was used for introducing substitutions, and protonation states were assigned with PROPKA² at pH 7.4. Using tleap from the Amber18 package of molecular simulation software⁵, the systems were neutralized by adding counter ions and solvated in an octahedral box of TIP3P water²⁷ with a minimal water shell of 12 Å around the protein.

MD simulations were performed with Amber18⁵. The ff14SB force field³⁷ was used to parameterize the protein, Joung-Chetham parameters²⁹ were used for the counter ions, and TIP3P²⁷ for the water. The fluorophore was parameterized using antechamber⁷², prepgen, and parmchk2, which are part of Amber18, following the procedure described here: http://ambermd.org/tutorials/basic/tutorial5/index.htm. See supplementary information for topology and force field information. To cope with long-range interactions, the Particle Mesh Ewald method¹⁰ was used; the SHAKE algorithm⁶² was applied to bonds involving hydrogen atoms. As hydrogen mass repartitioning²² was utilized, the time step for all MD simulations was 4 fs with a direct-space, non-bonded cutoff of 8 Å.

At the beginning, 17,500 steps of steepest descent and conjugate gradient minimization were performed; during 2,500, 10,000, and 5,000 steps, positional harmonic restraints with force constants of 25 kcal $\text{mol}^{-1} \, \text{Å}^{-2}$, 5 kcal $\text{mol}^{-1} \, \text{Å}^{-2}$, and zero, respectively, were applied to the solute atoms. Thereafter, 50 ps of NVT (constant number of particles,

volume, and temperature) MD simulations were conducted to heat up the system to 100 K, followed by 300 ps of NPT (constant number of particles, pressure, and temperature) MD simulations to adjust the density of the simulation box to a pressure of 1 atm and to heat the system to 300 K. During these steps, a harmonic potential with a force constant of 10 kcal mol⁻¹ Å⁻² was applied to the solute atoms. As the final step in thermalization, 300 ps of NVT-MD simulations were performed, while gradually reducing the restraint forces on the solute atoms to zero within the first 100 ps of this step. Afterward, five independent production runs of NVT-MD simulations with 2 μ s length each were performed. For this, the starting temperatures of the MD simulations at the beginning of the thermalization were varied by a fraction of a Kelvin.

Structures were extracted from the trajectories every 2 ns using cpptraj^{60,61}.

Constrained Network Analysis

The extracted structures were post-processed using Constraint Network Analysis (CNA)⁴⁸ as described in Nutschel *et al.*⁴⁴. In short, for analyzing the rigid cluster decomposition of all GFP variants, a constraint dilution simulation was performed using CNA on an ensemble of network topologies generated from an MD trajectory (ENT^{MD}). The ensemble-based CNA was pursued to increase the robustness of the rigidity analyses^{48,56}. Subsequently, the unfolding trajectory was visually inspected using VisualCNA⁵⁵ for identifying secondary structure elements that segregate from the largest rigid cluster at each major phase transition. VisualCNA is an easy-to-use PyMOL plugin that allows setting up CNA runs and analyzing CNA results, linking data plots with molecular graphic representations⁵⁵. See supplementary information for more details.

Functional properties

Fluorescence spectra

Spectral scans were performed using a plate reader (Clariostar, BMG Labtech, Ortenberg, Germany). Redox biosensor variants were diluted to 1 μ M protein concentration in potassium phosphate buffer (100 mM potassium phosphate, 100 mM NaCl, 0.5 mM Na₂-EDTA, pH 7.0). Sensor surface Cys were driven to full reduction using 10 mM dithiothreitol (DTT) or to full oxidation using 1 mM 2,2-dithiopyridylsulfide (DPS). Excitation scans were

recorded at 530 ± 10 nm emission, and emission scans after excitation at 405 ± 10 nm and 485 ± 10 nm, respectively. For measurements at 10 °C, pre-cooled buffer, recombinant proteins, and DTT/DPS stock solutions were used. For measurements at 37 °C the buffer and plate reader were preheated. Four technical replicates were performed.

Dynamic change of ratio

The different redox biosensor proteins (roGFP2, hGrx1-roGFP2, sfroGFP2^{WT}, and hGrx1-sfroGFP2) were pre-reduced using 10 mM DTT and desalted using Bio-Gel P-6 gel (Bio-Rad, Feldkirchen, Germany) resuspended in potassium phosphate buffer (100 mM potassium phosphate, 100 mM NaCl, 0.5 mM Na₂-EDTA, pH 7.0). Redox biosensors were diluted to a final concentration of 1 μ M protein in potassium phosphate buffer. Buffer and plate reader were preheated to 37 °C. Redox biosensors were excited sequentially at 400 \pm 10 nm and 482 \pm 16 nm with emission at 530 \pm 40 nm in a plate reader (Clariostar, BMG Labtech, Ortenberg, Germany). Fluorescence intensities were measured every 20 sec for 240 sec. After 80 sec at baseline measurement with pre-reduced sensor protein, 1 mM diamide (DIA) was added, and oxidation was monitored for 80 sec before reduction by adding 10 mM DTT. Ratios were plotted against time using GraphPadPrism8. Three independent repetitions were performed using sensor protein from three different batches.

pH response

The different redox biosensors were equilibrated in buffers adjusted to pH values ranging from 5.0–9.0. (pH 5.0 to pH 6.5, 10 mM MES-KOH, 100 mM NaCl, 5 mM EDTA; pH 7.0 to pH 8.0, 100 mM Hepes-KOH, 100 mM NaCl, 5 mM EDTA; pH 8.5 to pH 9.5, 100 mM Tris-HCL, 100 mM NaCl, 5 mM EDTA). Redox biosensor variants were excited sequentially at 400 ± 5 nm and 482 ± 8 nm in a plate reader (Clariostar, BMG Labtech, Ortenberg, Germany). All pH points were measured for oxidized (1 mM DPS) and reduced (10 mM DTT) sensor protein using four technical replicates each.

Redox titration

To determine the midpoint potentials, redox sensors were equilibrated (1 h) with DTT buffers (reduced form 1,4-dithiothreitol, DTT_{red} ; oxidized form 1,3-dithiane, DTT_{ox}). DTT_{red}/DTT_{ox} was used in a total concentration of 10 mM in degassed HEPES buffer (100

mM Hepes, 100 mM NaCl, 0.5 mM Na₂-EDTA, pH 7.0). The relation of DTT_{red} and DTT_{ox} to set a certain redox potential was calculated with the Nernst equation based on the standard reduction potential of DTT ($E^{0'}_{DTT}$), -330 mV (Equation 1).

$$E_{DTT} = E_{DTT}^{0'} - 2.303 \frac{RT}{zF} \log \frac{DTT_{red}}{DTT_{ox}}$$
 Eq.1

R is the gas constant (8.315 J K⁻¹ mol⁻¹); *T* is the absolute temperature (310.45 K); *z* is the number of transferred electrons (2); *F* is the Faraday's constant (96,485 C mol⁻¹).

Redox potentials ranging from -220 mV to -360 mV were adjusted. Additionally, redox sensors were fully reduced (10 mM DTT) and fully oxidized (1 mM DPS). Redox sensors were excited sequentially at 400 ± 5 nm and 482 ± 8 nm in a plate reader (Clariostar, BMG Labtech, Ortenberg, Germany). The degree of oxidation (OxD) was determined according to Equation 2.

$$OxD = \frac{R - R_{red}}{\frac{I_{48Sox}}{I_{nor...}}(R_{ox} - R) + (R - R_{red})}$$
 Eq.2

R represents the ratio of the fluorescence intensity measured at 405 nm and 485 nm $(R=\frac{405 \text{ nm}}{485 \text{ nm}})$; R_{red} and R_{ox} are the ratios of the fluorescence intensity of fully reduced or fully oxidized protein; $I_{485 \text{ nm}}$ is the fluorescence intensity at 485 nm for fully oxidized protein; $I_{485 \text{red}}$ is the fluorescence intensity at 485 nm for fully reduced protein.

To determine the midpoint potential $E^{0'}$ for the different roGFP2 variants, OxD_{roGFP2} was plotted against the calculated redox potential, which was adjusted with DTT_{red}/DTT_{ox} . Using GraphPadPrim8, all data points were fitted to a sigmoidal dose–response curve.

In cellulo characterization of redox biosensor variants

Spectral scan in cellulo

Spectral scans were performed using NF54*attB* parasites stably expressing hGrx1-roGFP2, sfroGFP2^{WT}, or hGrx1-sfroGFP2. Parasites were previously synchronized with 5% sorbitol. Trophozoite stage parasites were magnetically enriched and diluted in Ringer's solution (122.5 mM NaCl, 5.4 mM KCl, 1.2 mM CaCl₂, 0.8 mM MgCl₂, 11 mM D-glucose, 25 mM HEPES,1 mM NaH₂PO₄ pH 7.4) (100,000 parasites/μl). Parasites were fully reduced using 10

mM DTT or fully oxidized using 1 mM DIA. Emission and excitation scans were recorded using a plate reader (Clariostar, BMG Labtech, Ortenberg, Germany), with four technical repeats each. Spectra were plotted using GraphPadPrism8.

Western blot analysis

NF54attB^{hGrx1-roGFP2}, NF54attB^{sfroGFP2}, NF54attB^{hGrx1-sfroGFP2} parasites were synchronized using sorbitol. Trophozoite stage parasites were harvested via saponin lysis. After washing three times with phosphate-buffered saline (PBS), parasites were lysed using M-PER[™] buffer (ThermoFisher Scientific, Waltham, MA, USA). Parasite supernatants were mixed with 4x sample buffer with DTT and incubated for 5 min at 95 °C. Samples were separated using SDS-PAGE (sodium dodecyl sulfate-polyacrylamide gel electrophoresis) and blotted to a nitrocellulose membrane. After blocking with 5% milk, the membrane was incubated with an anti-GFP antibody (AB) (1:500 in 5% milk); an anti-mouse AB conjugated with HRP (horseradish peroxidase) was used as a secondary AB (1:10,000 in 5% milk). After the reaction with luminol, chemiluminescence was detected using an iNTAS ECL Chemostar. Then, the membrane was stripped using the restore TM PLUS western blot stripping buffer (ThermoFisher Scientific, Waltham, MA, USA). After blocking with 5% milk overnight, the membrane was incubated with an anti-HSP70 AB (1:500 in 5% milk) as a loading control. Anti-rabbit AB (1:2,000 in 5% milk) conjugated with HRP was used as a secondary AB. Chemiluminescence was detected as described above. Two biological replicates in two technical replicates were performed. Background subtraction using the rolling ball algorithm was performed with Fiji⁶³. Band intensities were measures using Fiji. GFP signal was normalized by the associated PfHSP70 loading control. Fold change of band intensity and the percentage change of the expression level between NF54attBhGrx1-roGFP2 and NF54attB^{sfroGFP2}, as well as NF54attB^{hGrx1-roGFP2} and NF54attB^{hGrx1-sfroGFP2}, were calculated.

CLSM imaging

To record CLSM images, parasites were prepared as described by Schuh *et al.*⁶⁴. Briefly, trophozoite stage parasites were magnetically enriched and washed with prewarmed (37 °C) Ringer's solution. Parasites were seeded on poly-L-lysine-coated μ -slides VI (ibidi). Images were taken using a Leica confocal system TCS SP5 inverted microscope equipped

with the objective HCX PL APO 63.0×1.30 GLYC 37 °C UV connected to a 37 °C temperature chamber. Samples were excited with a sequential scan at 405 nm and 488 nm; emission was detected at 500-550 nm. Scanning was performed at 400 Hz frequency and at a 512×512 pixel resolution. The argon laser power was set to 20%; smart gain and smart offset were 950 V and -0.9%, respectively. Images were processed using Fiji. The background was subtracted using the rolling ball algorithm, and contrast was enhanced by 0.01%. To improve the recognizability, colors from the green and red channels were set to yellow and magenta and merged.

Acknowledgments

The authors gratefully acknowledge Michaela Stumpf, Marie Sorg, and Norma Schulz for their technical assistance. Furthermore, we would like to thank Ilme Schlichting, and Miroslaw Tarnawski for the thoughtfully arranged data collection. Diffraction data was collected at beamline X10SA, Swiss Light Source, Paul Scherrer Institute, Villigen, Switzerland, and the authors thank the beamline staff for the excellent setup. We are grateful for computational support and infrastructure provided by the *Zentrum für Informations- und Medientechnologie* (ZIM) at the Heinrich Heine University Düsseldorf and the computing time provided by the John von Neumann Institute for Computing (NIC) to HG on the supercomputer JUWELS at Jülich Supercomputing Centre (JSC) (user ID: HKF7, VSK33).

Author Contributions:

KFW, KB, MS, HG, and JP directed the overall research program; KCH, CG, AKS, TN conducted the experiments; KFW, KCH, and CG analyzed the data and prepared figures; all authors contributed to experimental design and wrote and edited the manuscript.

Author Disclosure Statement

The authors have nothing to declare.

Funding statement

The German Research Foundation (SPP1710; to KB, MS, SR, and HG) and LOEWE Center DRUID (Project E3 to KB and SR) supported this study. The German Research Foundation funds the Center for Structural Studies (DFG Grant number 417919780).

Abbreviations

AA = amino acid; AB = antibody; avGFP = $Aequorea\ victoria\ GFP$; Cn^R = carbenicillin resistance; DIA = diamide; DPS = 2,2-dithiopyridylsulfide; DR, δ = dynamic range; DTT = dithiothreitol; DTT_{red} = 1,4-dithiothreitol; DTT_{ox} = 1,3-dithiane; FPLC = fast protein liquid chromatography; GFP = green fluorescent protein; hGrx1-roGFP2 = human glutaredoxin 1 fused to reduction/oxidation-sensitive green fluorescent protein; hGrx1-sfroGFP2 = human glutaredoxin 1 fused to superfolder reduction/oxidation-sensitive green fluorescent protein; HRP = horseradish peroxidase; Kan^R = kanamycin resistance; LB = lysogeny broth; OxD = degree of oxidation; PBS = phosphate-buffered saline; PEG = polyethylene glycol; P. $falciparum = Plasmodium\ falciparum$; PMSF = phenylmethylsulfonyl fluoride; rmsd = rootmean-square deviation; roGFP2 = reduction/oxidation-sensitive green fluorescent protein; ROS = reactive oxygen species; RT = room temperature; s = second; SDS-PAGE = sodium dodecyl sulfate—polyacrylamide gel electrophoresis; s = superfolding; s = sofoFP2 = superfolder reduction/oxidation-sensitive green fluorescent protein; TB = terrific broth; FI = fluorescence intensity; s = glutaredoxin 1; s = human glutaredoxin 1; WB = Western blot; s = isosbestic point

References

- Adams PD, Afonine PV, Bunkoczi G, Chen VB, Davis IW, Echols N, Headd JJ, Hung LW, Kapral GJ, Grosse-Kunstleve RW, McCoy AJ, Moriarty NW, Oeffner R, Read RJ, Richardson DC, Richardson JS, Terwilliger TC, and Zwart PH. PHENIX: a comprehensive Python-based system for macromolecular structure solution. Acta Crystallogr D Biol Crystallogr 2010,66(2): 213-221.
- 2. Bas DC, Rogers DM, and Jensen JH. Very fast prediction and rationalization of pKa values for protein-ligand complexes. Proteins 2008,73(3):765-783.
- 3. Brejc K, Sixma TK, Kitts PA, Kain SR, Tsien RY, Ormö M, and Remington SJ. Structural basis for dual exitation and photoisomerization of the *Aequorea victoria* green fluorescent protein. Proc Natl Acad Sci U S A 1997,94(6):2306-2311.
- 4. Campbell BC, Petsko GA, and Liu CF. Crystal structure of green fluorescent protein lover and design of clover-based redox sensors. Structure 2018,26(2):225-237.
- 5. Case DA, Brozell SR, Cerutti DS, Cheatham TE, Cruzeiro VWD III, Darden TA, Duke RE, Ghoreishi D, Gohlke H, Goetz AW, Greene D, Harris R, Homeyer N, Izadi S, Kovalenko A, Lee TS, LeGrand S, Li P, Lin C, Liu J, Luchko T, Luo R, Mermelstein DJ, Merz KM, Miao Y, Monard G, Nguyen H, Omelyan I, Onufriev A, Pan F, Qi R, Roe DR, Roitberg A, Sagui C, Schott-Verdugo S, Shen J, Simmerling CL, Smith J, Swails J, Walker RC, Wang J, Wei H, Wolf RM, Wu X, Xiao L, York DM, and Kollman PA. AMBER 2018. University of California, San Francisco, 2018.
- 6. Chaturvedi D, and Mahalakshmi R. Transmembrane β-barrels: evolution, folding and energetics. Biochim Biophys Acta Biomembr 2017,1859(12):2467-2482.
- 7. Cormack BP, Valdivia RH, and Falkow S. FACS-optimized mutants of the green fluorescent protein (GFP). Gene 1996,173:33-38.
- 8. Crameri A, Whitehorn EA, Tate E, and Stemmer WPC. Improved green fluorescent protein by molecular evolution using DNA shuffling. Nat Biotechnol 1996,14(3):315-9.
- 9. Dahiyat BI, Gordon DB, and Mayo SL. Automated design of the surface positions of protein helices. Protein Sci 1997,6(6):1333–1337.

- 10. Darden T, York D, and Pedersen L. Particle mesh Ewald: an N.log(N) method for ewald sums in large systems. J Chem Phys 1993,98(12):10089-10092.
- 11. Deller MC, Kong L, Rupp B. Protein stability: a crystallographer's perspective. ACTA Crystallogr F, 2016,72:72-95.
- 12. Dooley CT, Dore TM, Hanson GT, Jackson WC, Remington SJ, and Tsien RY. Imaging dynamic redox changes in mammalian cells with green fluorescent protein indicators. J Biol Chem 2004,279(21):22284-22293.
- 13. Dooley CT, Li L, Misler JA, and Thompson JH. Toxcicity of 6-hydroxydopamine: live cell imaging of cytoplasmic redox fluc. Cell Biol Toxicol 2012,28:89-101.
- 14. Emsley P, Lohkamp B, Scott WG, and Cowtan K. Features and development of Coot.

 Acta Crystallogr D Biol Crystallogr 2010,66(4):486-501.
- 15. Folch B, Rooman M, and Dehouck Y. Thermostability of salt bridges versus hydrophobic interactions in proteins probed by statistical potentials. J Chem Inf Model 2008,48:119–127.
- 16. Fujita K, and Ohno H. Enzymatic activity and thermal stability of metallo proteins in hydrated ionic liquids. Biopolymers 2010,93(12):1093-1099.
- 17. Gutscher M, Pauleau AL, Marty L, Brach T, Wabnitz GH, Samstag Y, Meyer AJ, and Dick TP. Real-time imaging of the intracellular glutathione redox potential. Nat Methods 2008,5(6):553-559.
- 18. Hanson GT, Aggeler R, Oglesbee D, Cannon M, Capaldi RA, Tsien RY, and Remington SJ. Investigating mitochondrial redox potential with redox-sensitive green fluorescent protein indicators. J Biol Chem 2004,279(13):13044-13053.
- 19. Heim R, Prasher DC, Tsien RY. Wavelength mutations and prosttranslational autoxidation of green fluorescent protein. Biochemistry 1994,91:12501-12504.
- 20. Hermans SM, Pfleger C, Nutschel C, Hanke CA, and Gohlke H. Rigidity theory for biomolecules: concepts, software, and applications. Wiley Interdiscip Rev Comput Mol Sci. 7(e1311), 2017.
- 21. Hespenheide B, Jacobs D, and Thorpe M. Structural rigidity in the capsid assembly of cowpea chlorotic mottle virus. J Phys: Condens Matter 2004,16(S5055).

- 22. Hopkins CW, Le Grand S, Walker RC, and Roitberg AE. Long-Time-Step Molecular Dynamics through Hydrogen Mass Repartitioning. J Chem Theory Comput 2015,11(4):1864-1874.
- 23. Ilmberger N, Meske D, Juergensen J, Schulte M, Barthen P, Rabausch U, Angelov A, Mientus M, Liebl W, Schmitz RA, and Streit WR. Metagenomic cellulases highly tolerant towards the presence of ionic liquids—linking thermostability and halotolerance. Appl Micriobiol Biot 2012,95(1):135-146.
- 24. Jacobs DJ, and Thorpe MF. Generic rigidity percolation: the pebble game. Phys. Rev. Lett. 1995,75(22):4051.
- 25. Jacobs DJ, Rader AJ, and Kuhn LA. Protein flexibility predictions using graph theory. Proteins 2001,4(2): 150-165.
- 26. Jacobs DJ. Generic rigidity in three-dimensional bond-bending networks. J Phys A: Math Gen. 1998,31(6653).
- 27. Jorgensen WL, Chandrasekhar J, Madura JD, Impey RW, and Klein ML. Comparison of simple potential functions for simulating liquid water. J Chem Phys 1983,79(2):926-935.
- 28. Jortzik E, Becker K. Thioredoxin and glutathione systems in *Plasmodium* falciparum. Int J Med Microbiol 2012,302:187-194.
- 29. Joung IS, and Cheatham TE III. Determination of alkali and halide monovalent ion parameters for use in explicitly solvated biomolecular simulations. J Phys Chem B 2008,112(30):9020-9041.
- 30. Kabsch W. Integration, scaling, space-group assignment and post-refinement. Acta Crystallogr D Biol Crystallogr 2010,66(2):133-144.
- 31. Karshikoff A, Nilsson L, and Ladenstein R. Rigidity versus flexibility: the dilemma of understanding protein thermal stability. FEBS J 2015,282(20):3899-3917.
- 32. Kasozi D, Mohring F, Rahlfs S, Meyer AJ, and Becker K. Real-time imaging of the intracellular glutathione redox potential in the malaria parasite *Plasmodium* falciparum. PLoS Pathog 2013, 9(12):e1003782.
- 33. Kavishe RA, Koenderik JB, and Alifrangis M. Oxidative stress in malaria and artemisinin combination therapy: Pros and Cons. FEBS J 2017,284:2579-2591.

- 34. Krüger DM, Rathi PC; Pfleger C, and Gohlke H. CNA web server: rigidity theory-based thermal unfolding simulations of proteins for linking structure, (thermo-) stability, and function. Nucleic Acids Res 2013,41:W340–W348.
- 35. Lakowicz JR, ed. Principles of fluorescence spectroscopy. Springer Science & Business Media, 2013.
- 36. LaVallie ER, Lu Z, Diblaso-Smith EA, Collins-Racie LA, and McCoy JM. Thioredoxin as a fusion partner for production of soluble recombinant proteins in Escherichia coli. Method Enzymol 2000,326:322.
- 37. Maier JA, Martinez C, Kasavajhala K, Wickstrom L, Hauser KE, and Simmerling C. ff14SB: Improving the Accuracy of Protein Side Chain and Backbone Parameters from ff99SB. J Chem Theory Comput 2015,11(8):3696-3713.
- 38. Mann JP, McCluskey A, and Atkin R. Activity and thermal stability of lysozyme in alkylammonium formate ionic liquids—influence of cation modification. Green Chem 2009,11(6):785-792.
- 39. Meyer AJ, and Dick TP. Fluorescent protein-based redox probes. Antioxid Redox Sign 2010,13(5):621-650.
- 40. Minton AP. How can biochemical reaction within cells differ from those in tubes? J Cell Sci 2006,119:2863-2869.
- 41. Nakatani T, Yasui N, Tamura I, and Yamahita A. Specific modification at the C-terminal lysine residue of the green fluorescent protein variant, GFPuv, expressed in Escherichia coli. Sci Rep 2019,9(1): 1-13.
- 42. Naveed H, and Liang J. Weakly stable regions and protein-protein interactions in beta-barrel membrane proteins. Curr Pharm Des 2014,20(8):1268-1273.
- 43. Nkrumah LJ, Muhle RA, Moura PA, Ghosh P, Hatfull GF, Jacobs WR, Fidock DA.

 Efficient site-specific integration in *Plasmodium falciparum* chromosomes

 mediated by mycobacteriophage Bxb1 integrase. Nat Methods 2006,3(8):615-621.
- 44. Nutschel C, Fulton A, Zimmermann O, Schwaneberg U, Jaeger K-E, Gohlke H. Systematically scrutinizing the impact of substitution sites on thermostability and detergent tolerance for Bacillus subtilis lipase A. J Chem Inf Model 2020,60(3):1568-1584.

- 45. Pédelacq JD, Cabantous S, Tran T, Terwilliger TC, and Waldo GS. Engineering and characterization of a superfolder green fluorescent protein. Nat Biotechnol 2006,24(1):79-88.
- 46. Pérez VI, Buffenstein R, Masamsetti V, Leonard S, Salmon AB, Mele J, Andziak B, Yang T, Edrey Y, Friguet B, Ward W, Richardson A, and Chaudhuri A. Protein stability and resistance to oxidative stress are determinants of longevity in the longest-living rodent, the naked mole-rat. PNAS 2009,106(9):3059-3064.
- 47. Pettersen E F, Goddard TD, Huang CC, Couch GS, Greenblatt DM, Meng EC, and Ferrin TE. UCSF Chimera--a visualization system for exploratory research and analysis. J Comput Chem 2004,25(13):1605-1612.
- 48. Pfleger C, and Gohlke H. Efficient and robust analysis of biomacromolecular flexibility using ensembles of network topologies based on fuzzy noncovalent constraints. Structure 2013,21(10):1725-1734.
- 49. Pfleger C, Radestock S, Schmidt E, and Gohlke H. Global and local indices for characterizing biomolecular flexibility and rigidity. J Comput Chem 2013a,34.(3): 220-233.
- 50. Pfleger C, Rathi PC, Klein DL, Radestock S, and Gohlke H. Constraint Network Analysis (CNA): a Python software package for efficiently linking biomacromolecular structure, flexibility, (thermo-) stability, and function. J Chem Inf Model 2013,53(4):1007-1015.
- 51. Prasher DC, Eckenrode VK, Ward WW, Prendergast FG, and Cormier MJ. Primary structure of the *Aequorea victoria* green-fluorescent protein. Gene 1992,111(2):229-233.
- 52. Privalov PL and Gill SJ. Stability of protein structure and hydrophobic interaction.

 Adv Protein Chem 1988,39:191–234.
- 53. Radestock S and Gohlke H. Protein rigidity and thermophilic adaptation. Proteins. 2011,79(4):1089–1108.
- 54. Radestock S, Gohlke H. Exploiting the link between protein rigidity and thermostability for data-driven protein engineering. Eng Life Sci 2008,8(5):507–522.

- 55. Rathi PC, Mulnaes D, and Gohlke H. VisualCNA: a GUI for interactive constraint network analysis and protein engineering for improving thermostability. Bioinformatics 2015,31(14):2394-2396.
- 56. Rathi PC, Radestock S, Gohlke H. Thermostabilizing mutations preferentially occur at structural weak spots with a high mutation ratio. J Biotechnol 2012,159(3):135–144.
- 57. Rathi, PC, Fulton A, Jaeger K-E, Gohlke H. Application of rigidity theory to the thermostabilization of lipase A from Bacillus subtilis. PLoS Comput Biol 2016,12:e1004754.
- 58. Rathi, PC, Jaeger K-E, and Gohlke H. Structural rigidity and protein thermostability in variants of lipase A from Bacillus subtilis. PLOS ONE 2015a,10:e0130289.
- 59. Rivas G, Minton AP. Macromolecular crowding in vitro, in vivo, an in between. Trends Biochem Sci 2016,41(11):970-981.
- 60. Roe DR, and Cheatham TE III. Parallelization of CPPTRAJ enables large scale analysis of molecular dynamics trajectory data. J Comput Chem 2018,39(25):2110-2117.
- 61. Roe DR, and Cheatham TE III. PTRAJ and CPPTRAJ: software for processing and analysis of molecular dynamics trajectory data. J Chem Theory Comput 2013,9(7):3084-3095.
- 62. Ryckaert JP, Ciccotti G, and Berendsen HJC. Numerical-Integration of Cartesian Equations of Motion of a System with Constraints Molecular-Dynamics of N-Alkanes. J Comput Phys 1977,23(3):327-341.
- 63. Schindelin J, Arganda-Carreras I, Frise E, Kaynig V, Longair M, Pietzsch T, Preibisch S, Rueden C, Saalfeld S, Schmid B, Tinevez J-Y, White DJ, Hartenstein V, Eliceiri K, Tomancak P, and Cardona A. Fiji: an open-source platform for biological-image analysis. Nat Methods 2012,9(7):676–682.
- 64. Schuh AK, Rahbari M, Heimsch KC, Mohring F, Gabryszewski SJ, Weder S, Buchholz K, Rahlfs S, Fidock DA, and Becker K. Stable integration and comparison of hGrx1-roGFP2 and sfroGFP2 redox probes in the malaria parasite *Plasmodium falciparum*. ACS Infect Dis 2018,4:1601-1612.

- 65. Schwarzländer M, Dick TP, Meyer AJ, and Morgan B. Dissecting redox biology using fluorescent protein sensors. Antioxid redox sign 2016,24(13):680-712.
- 66. Shimomura O, Johnson FH, Saiga Y. Extraction, purification and properties of aequorin, a bioluminescent protein from the luminous hydromedusan, *Aequorea*. J Cell Comp Physiol 1962,59:223-239.
- 67. Shimomura O. Structure of the chromophore of *Aequorea* green fluorescent protein. FEBS LETT 1979,104(2):220-222.
- 68. Sturm N, Hu Y, Zimmermann H, Fritz-Wolf K, Wittlin S, Rahlfs S, and Becker K. Compound structurally related to ellagic acid show improved antiplasmodial activity. Antimicrob Agents Ch 2009,53(2):622-630.
- 69. Trager W, and Jensen JB. Human malaria parasites in continuous culture. Science 1976,193:673-675.
- 70. Waldo GS, Standish BM, Berendzen J, and Terwilliger TC. Rapid protein-folding assay using green fluorescent protein. Nat Biotechnol 1999,17:691-695.
- 71. Wang J, Wang W, Kollman PA, and Case DA. Antechamber: an accessory software package for molecular mechanical calculations. J Am Chem Soc 2001,222:U403.
- 72. Waterhouse A, Bertoni M, Bienert S, Studer G, Tauriello G, Gumienny R, Heer FT, de Beer TAP, Rempfer C, Bordoli L, Lepore R, and Schwede T. SWISS-MODEL: homology modelling of protein structures and complexes. Nucleic Acids Res 2018,46(1):296-303.
- 73. Whiteley W. Counting out to the flexibility of molecules. Phys Biol 2005,2(4):S116.

Figure Legends

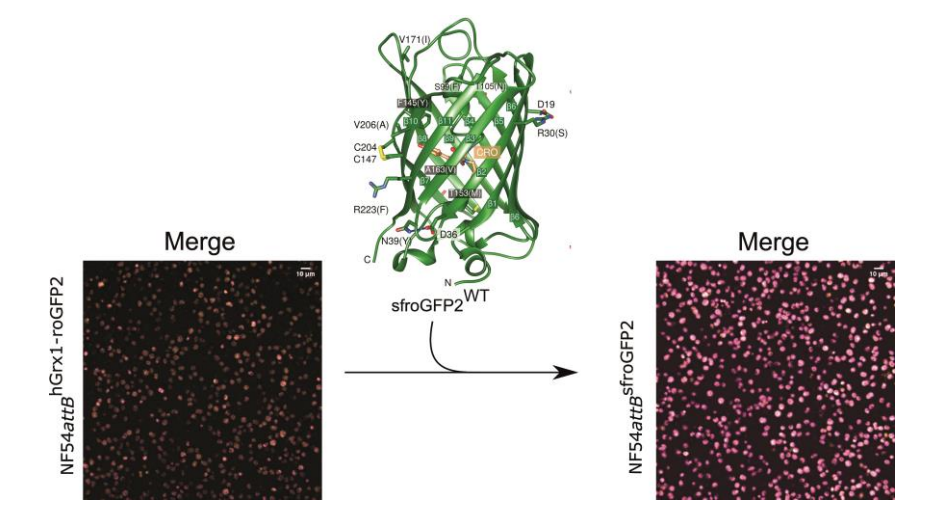


Figure 1: Graphical abstract. Comparison of trophozoite stage NF54attB P. falciparum parasites expressing hGrx1-roGFP2 or sfroGFP2. 405 nm and 488 nm images were taken with a confocal microscope and merged. Channel colors were set as yellow (405 nm) and magenta (488 nm). Both images were treated identically.

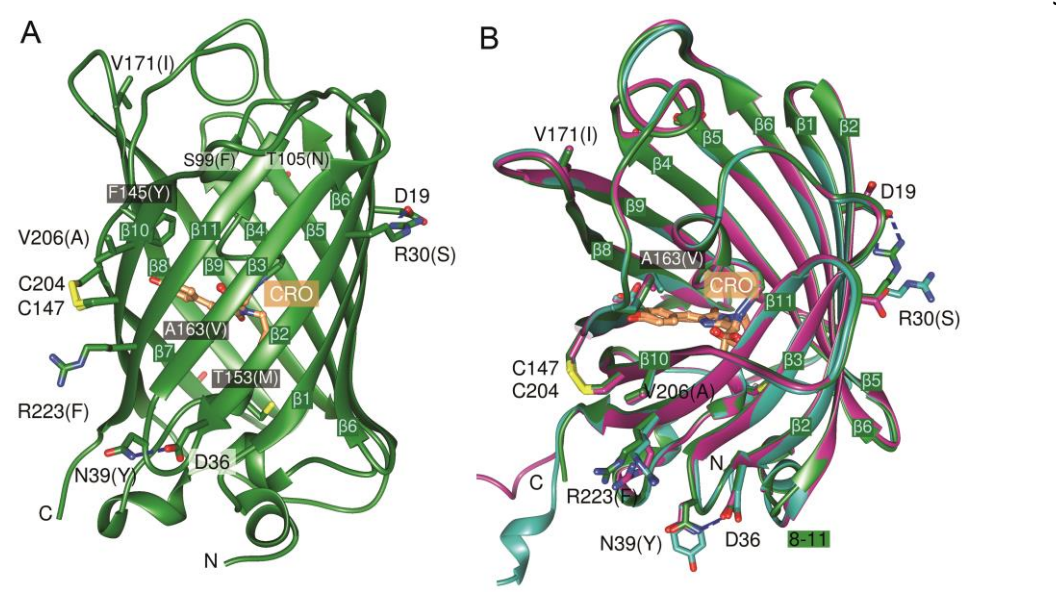


Figure 2: X-ray crystal structure analysis of sfroGFP2^{WT}, sfroGFP2^{R3OS}, and sfroGFP2^{N39Y}. A Model of sfroGFP2^{WT} based on X-ray crystal structure analysis. The protein crystal diffracted to a resolution of 1.1 Å. The structure was solved via molecular replacement. The two cysteines C147 and C204 form a disulfide bridge (represented in yellow). The chromophore is shown in orange. All sf mutations and the both cysteine mutations, which are elementary for the usage of GFP as a redox sensor, are labeled. The letter in brackets indicates the AA in the original roGFP2. Furthermore, the N and C-termini are labeled. CRO = chromophore. **B** Structural comparison between sfroGFP2^{WT} (green), sfroGFP2^{R3OS} (magenta), and sfroGFP2^{N39Y} (turquoise). The sfroGFP2^{R3OS} and sfroGFP2^{N39Y} crystals diffracted to a resolution of 1.4 Å and 2.0 Å, respectively. All structures were solved via molecular replacement. The individual β–strands are labeled. The main structural differences between the three variants occur at the N-terminus and in the loop region 8-11.

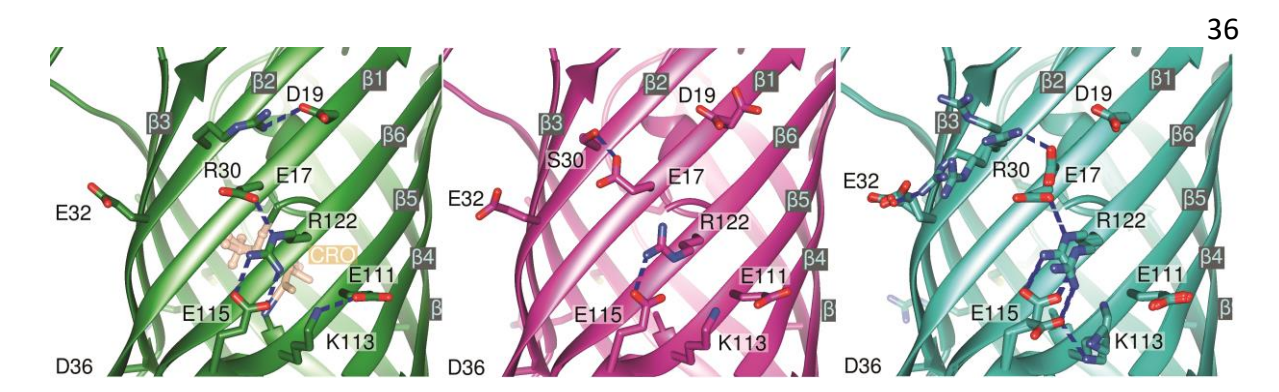


Figure 3: Close-up of sfroGFP2^{WT} (green), sfroGFP2^{R30S} (magenta), and sfroGFP2^{N39Y} (turquoise). Close-up of the individual barrel centers. Differences in the surroundings of residue R30 (sfroGFP2^{WT} and sfroGFP2^{N39Y}) or S30 (sfroGFP2^{R30S}) result in changes in the network of ionic interactions.

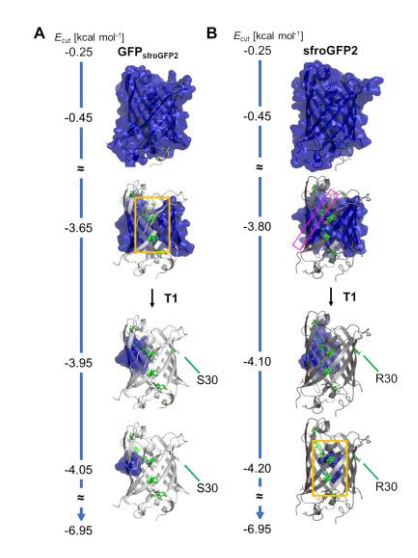


Figure 4: Constraint dilution trajectory of GFP_{sfroGFP2} (A) and sfroGFP2^{WT} (B) showing one major phase transition. The blue-colored body shows the largest rigid cluster over various energies with the major phase transition T1 indicated with a black arrow. $GFP_{sfroGFP2}$ (light gray) and $sfroGFP2^{WT}$ (dark gray) are shown as cartoons with residues affected by the roGFP2 (salmon) and sf (green) mutations shown as sticks. The pink rectangle indicates the β-strand (residues 142-151) that first loses structural stability. Close-ups of $GFP_{sfroGFP2}$ (see Figure 5A) and $sfroGFP2^{WT}$ (see Figure 5C) are indicated with orange rectangles.

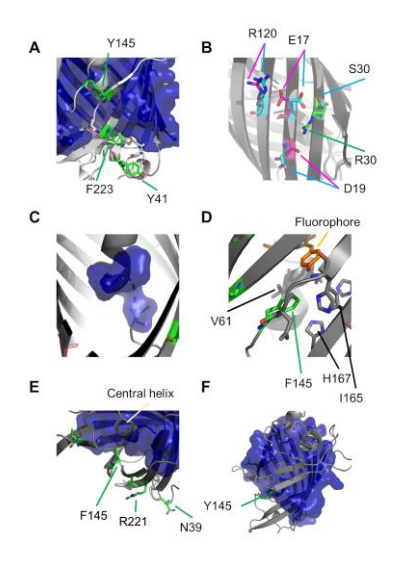


Figure 5: Close-ups of GFP_{sfroGFP2} and sfroGFP2^{WT} during constraint dilution simulations.

The blue-colored body shows the largest rigid cluster in GFP_{sfroGFP2} (light gray cartoon, **A**), sfroGFP2^{WT} (dark gray cartoon, **B-E**), and roGFP2 (medium gray, **B**, **F**), with the residues affected by the roGFP2 (salmon) and sf (green) mutations shown as sticks. In panel **A**, the state of GFP_{sfroGFP2} right before the transition point is shown. In panel **B**, roGFP2_{sfroGFP2} and sfroGFP2^{WT} are superimposed. The presence of the sf mutations (green, S30 in roGFP2, R30 in sfroGFP2^{WT}) leads to a different network of the surrounding residues in sfroGFP2^{WT} (magenta) than in roGFP2 (light blue). In panel **C**, the fluorophore is the last rigid structure in sfroGFP2^{WT}. In panel **D**, the sf mutation Y145F resides in a hydrophobic environment close to the fluorophore. In panel **E**, as a result, the β -strand containing Y145F percolates from the largest rigid cluster in sfroGFP2^{WT}. In panel **F**, a similar behavior of roGFP2 can be seen in which the β -strand containing Y145 percolates from the largest rigid cluster in roGFP2, while most of the β -barrel, including the chromophore and the central helix, remain rigid.

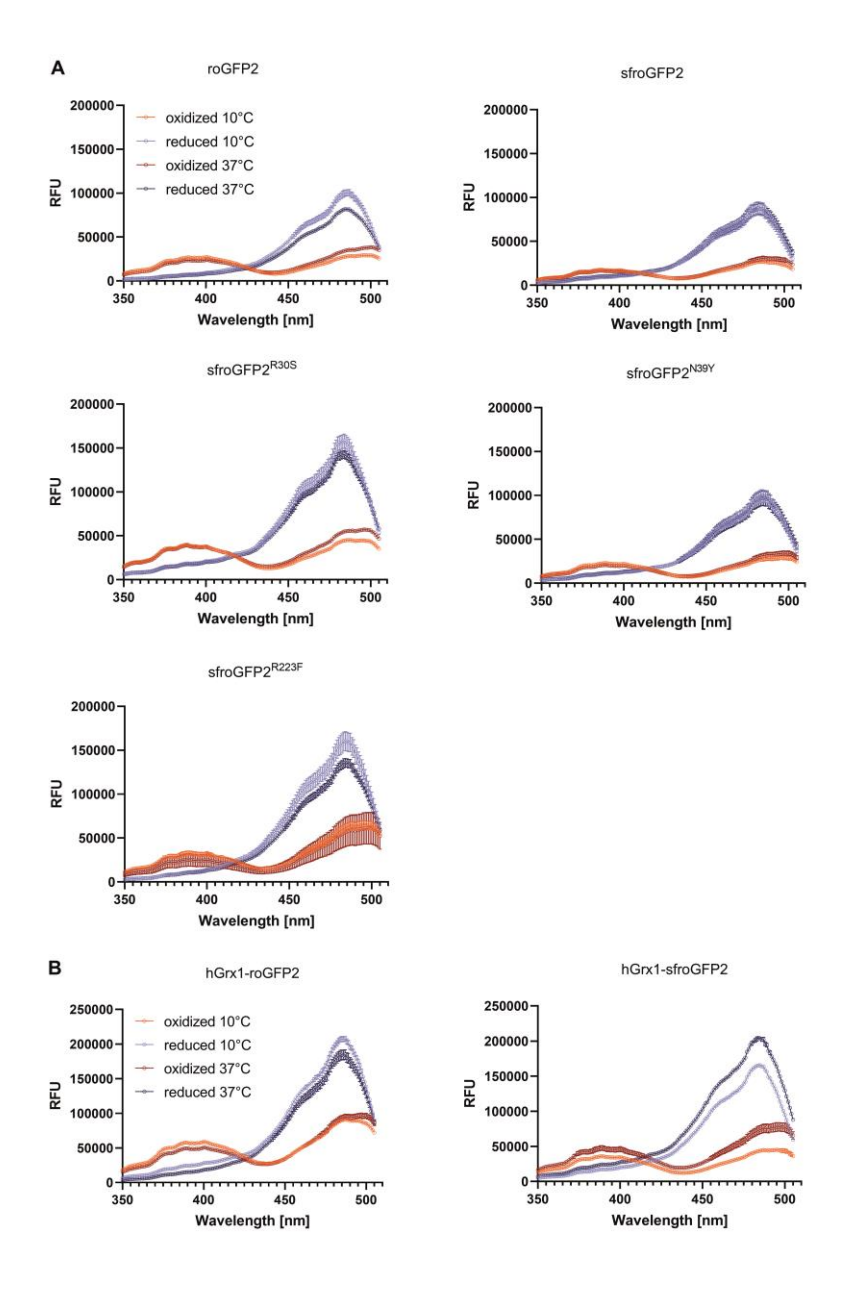


Figure 6: Spectral excitation scans of various redox biosensor variants. A Spectral excitation scans of sfroGFP2^{WT}, sfroGFP2^{R30S}, sfroGFP2^{N39Y}, and sfroGFP2^{R223F} in comparison to roGFP2. Sensors were fully oxidized using 1 mM 2,2 dithiopyridylsulfide (DPS) (red curves) or fully reduced using 10 mM dithiothreitol (DTT) (blue curves) prior to measurement. B Spectral excitation scans of hGrx1-roGFP2 and hGrx1-sfroGFP2. Sensors were fully oxidized using 1 mM DPS (red curves) or fully reduced using 10 mM DTT (blue curves). Light red and light blue spectra indicate measurements carried out at around 10 °C; dark red and dark blue spectra indicate measurements carried out at 37 °C. RFU = random fluorescence intensity units. For details, please see the Methods section.

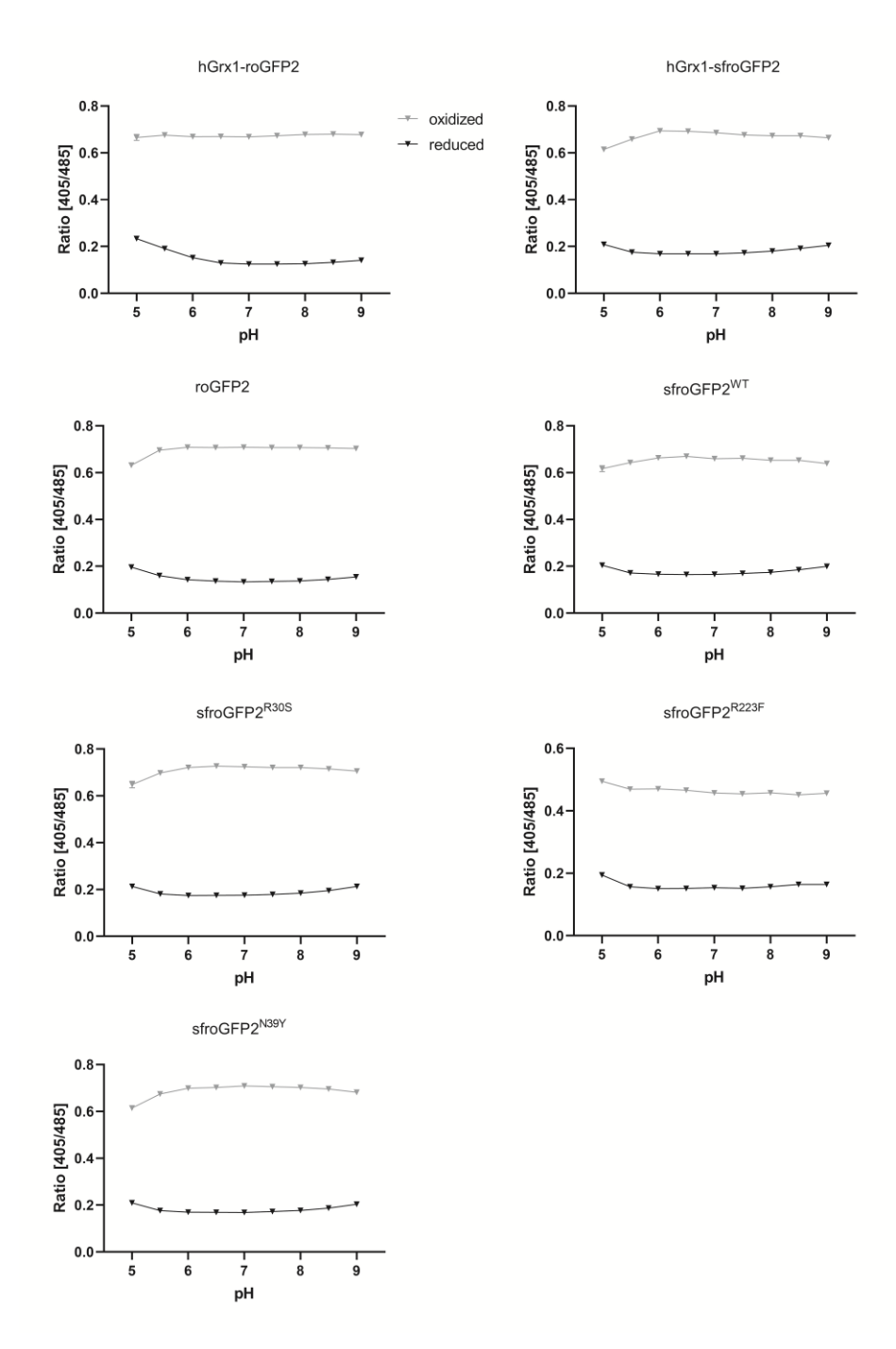


Figure 7: pH response of different biosensor variants. Recombinant sensor proteins were equilibrated in buffers with pH values varying between pH 5.0 and pH 9.0. All biosensor proteins were fully reduced and fully oxidized using 10 mM dithiothreitol (DTT) (black) and 1 mM 2,2 dithiopyridylsulfide (DPS) (grey), respectively. Their ratio $(R = \frac{405 \text{ nm}}{485 \text{ nm}})$ was measured using a clariostar plate reader and plotted over pH values of the buffers. Means \pm SD are shown. N = 4.

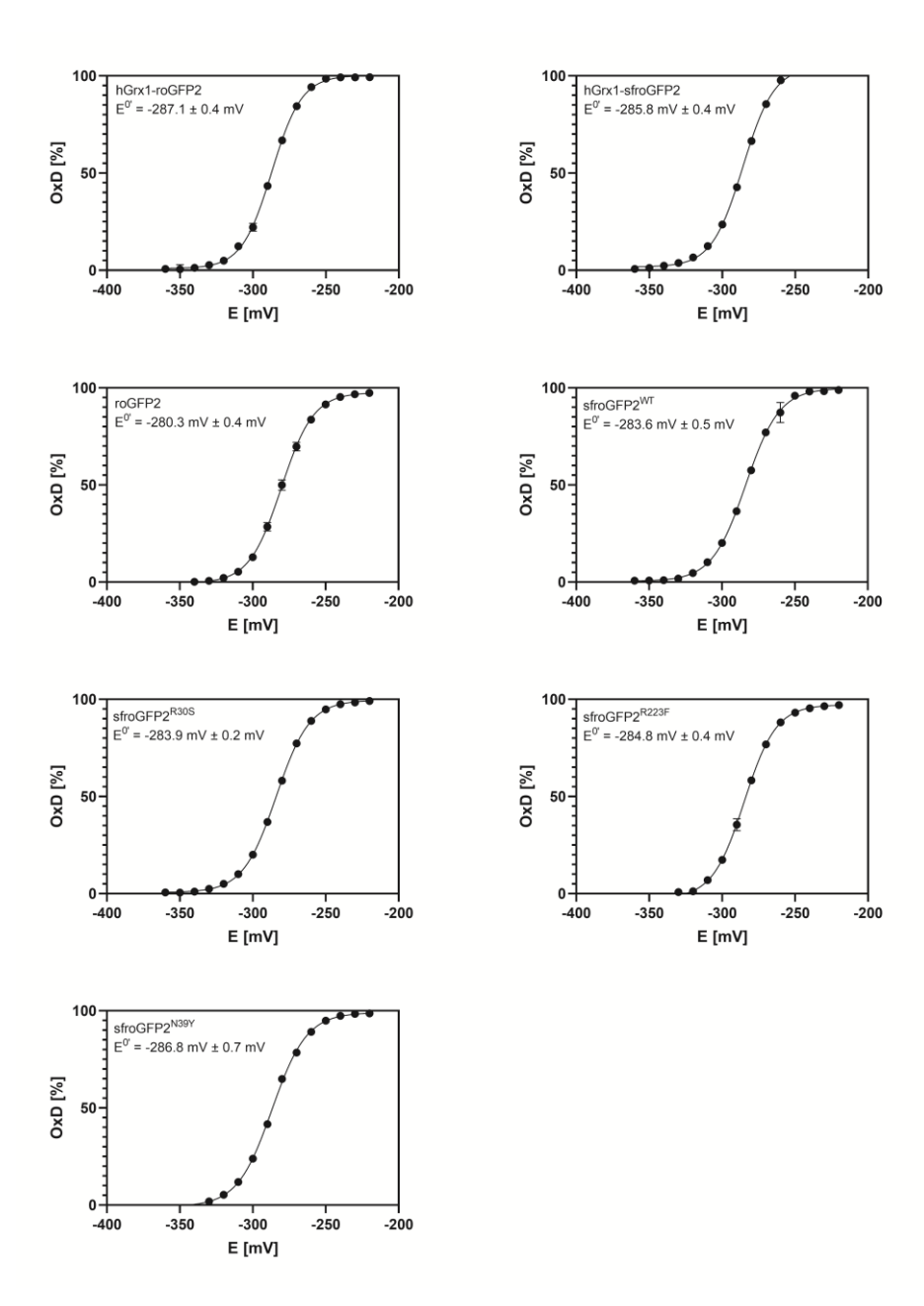
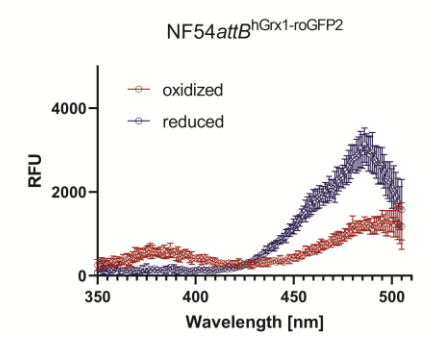


Figure 8: Redox titration of different biosensor variants. Specific redox potentials were adjusted using different mixtures of dithiothreitol (DTT_{red}) and dithian (DTT_{ox}), calculated from the Nernst equation. Biosensor proteins were allowed to equilibrate in the different buffers and were additionally fully reduced (10 mM DTT) and fully oxidized (1 mM DPS). Means with error bars indicating standard deviation are shown. N = 4.



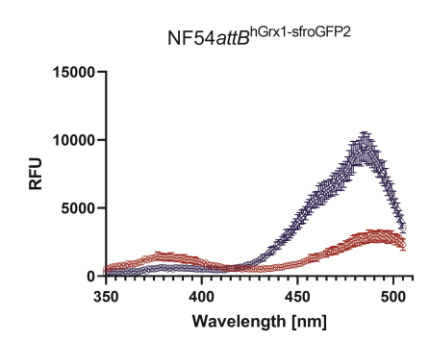


Figure 9: Spectral excitation scans of NF54attB^{hGrx1-roGFP2} and NF54attB^{hGrx1-sfroGFP2}. For spectral excitation scans, the sensor was fully reduced by treating the parasites with 10 mM dithiothreitol (DTT) (blue curve) and fully oxidized via treatment with 1 mM diamide (DIA) (red curve). $2.0x\ 10^6$ parasites each per measurement were used. RFU = random fluorescence intensity units. Mean and standard deviation from four independent replications are shown.

Table 1: Crystallogra						
	sfroGFP2 ^{WT}	sfroGFP2 ^{R30S}	sfroGFP2 ^{N39Y}			
Space group	P 2 ₁ 2 ₁ 2 ₁	P 1 2 ₁ 1	P 1 2 ₁ 1			
Unit cell parameters						
a, b, c (Å)	36.87, 47.37, 117.74	51.11, 68.92, 68.45	91.85, 51.29, 101.46			
α, β, γ (°)	90, 90, 90	90, 104.038, 90	90, 102.282, 90			
Data collection						
Beamline	SLS beam line X10SA	SLS beam line X10SA	SLS beam line X10SA			
Temperature (K)	100	100	100			
Wavelength (Å)	1	0.9998	0.9998			
Resolution range	19.85 - 1.05 (1.09 1.05)	45.35 - 1.35 (1.4 - 1.35)	47.92 – 2.0 (2.07 – 2.0)			
Wilson B-factor	8.9	17.2	26.7			
Total reflections	391518 (10387)	483809 (19241)	144797 (15047)			
Unique reflections	89058 (4957)	95798 (6718)	59713 (5842)			
Multiplicity	4.4 (2.1)	5.1 (2.9)	2.4 (2.6)			
Completeness (%)	91.7 (51.7)	94.8 (66.9)	94.5 (93.0)			
Mean I /σ (I)	16.2 (2.6)	17.7 (2.4)	6.8 (3.6)			
R-merge ^a (%)	4.4 (29.5)	4.5 (37.8)	7.5 (20.6)			
R-pim ^b (%)	2.3 (21.4)	2.1 (24.6)	5.7 (15.2)			
CC1/2 (%)	99.9 (88.6)	99.9 (87.0)	99.1 (96.2)			

			44	
Molecules per ASU	1	2	4	
Refinement				
R _{work} /R _{free} c (%)	14.9 (24.5) / 16.2		25.0 (25.5) / 29.9	
	(29.0)		(31.1)	
No. of atoms/averag				
Protein	1833	3773	7379	
Ligands	50	82	173	
Solvent	281	348	521	
Non-hydrogen atoms	2164	4203	8017	
Protein residues	229	473	927	
Ramachandran plot (
Favored (%)	99.1	99.1	98.2	
Outliers (%)	0.00	0.00	0.00	
Standard geometry (RMSZ)			
Bonds lengths	0.54	0.61	0.25	
Bond angles	0.75	0.80	0.47	
PDB accession code	7PCA	7PCZ	7PD0	
Statistics for the high	n-resolution shell are	e shown in parentheses.		
^a $R_{\text{merge}} = \sum_{hkl} \sum_{i} I_{i}(hkl) $	$[I(hkl)] / \sum_{hkl} \sum_{i} I_{i}(hkl)$, where I;(hkl) is the ith		
measurement of refl	ection <i>hkl</i> and [<i>I</i> (<i>hk</i>)	/)] is the weighted mean of all		
mea- surements;				
${}^{b}R_{\text{pim}} = \sum_{hkl} [1/(N 1$.)] 1/2 ∑ _i I _i (hkI) [I	$(hkl)] /\sum_{hkl}\sum_{i}l_{i}(hkl),$ where N is		

the redundancy for the hkl reflection;

 ${}^{c}R_{\text{work}}/R_{\text{free}} = \sum_{hkl} |F_{\text{o}}F_{\text{c}}|/\sum_{hkl}|F_{\text{o}}|$, where F_{c} is the calculated and F_{o} is the observed structure-factor amplitude of reflection hkl for the working/free (5%) set, respectively.

Table 2: Energies of major phase transitions of the investigated variants.

	sfroGFP2 ^{WT}	GFP _{sfroGFP2}	$roGFP2_{sfroGFP2}$	$R30S_{sfroGFP2}$	$N39Y_{sfroGFP2} \\$	R223F _{sfroGFP2}
$E_{cut}^{1,2}$	-4.01	-3.88	-4.04	-3.89	-4.07	-3.98
SEM ^{2,3}	0.07	0.08	0.02	0.03	0.08	0.05

¹ Values are averaged over all snapshots of n = 5 replicas with N = 5,000 snapshots each.

² In kcal mol⁻¹.

³ Standard error of the mean across five replicas